J Mar Sci Technol (2009) 14:200–213
DOI 10.1007/s00773-008-0031-4

ORIGINAL ARTICLE

Two-dimensional numerical simulation and experiment on strongly nonlinear wave–body interactions

Changhong Hu · Masashi Kashiwagi

Received: 30 October 2007 / Accepted: 10 July 2008 / Published online: 29 August 2008

Abstract A constrained interpolation profile (CIP)-based Cartesian grid method for strongly nonlinear wave–body interaction problems is presented and validated by a newly designed experiment, which is performed in a two-dimensional wave channel. In the experiment, a floating body that has a rectangular section shape is used. A superstructure is installed on the deck and a small floating-body freeboard is adopted in order to easily obtain water-on-deck phenomena. A forced oscillation test in heave and a wave–body interaction test are carried out. The numerical simulation is performed by the CIP-based Cartesian grid method, which is described in this paper. The CIP scheme is applied in the Cartesian grid-based flow solver. New improvements of the method include an interface-capturing method that applies the tangent of hyperbola for interface capturing (THINC) scheme and a virtual particle method for the floating body. The efficiency of the THINC scheme is shown by a dam-breaking computation. Numerical simulations on the experimental problem for both the forced oscillation test and the wave–body interaction test are carried out, and the results are compared to the measurements. All of the comparisons are reasonably good. It is shown, based on the numerical examples, that the present CIP-based Cartesian grid method is an accurate and efficient method for predicting strongly nonlinear wave–body interactions.

C. Hu (✉)
RIAM, Kyushu University, 6-1 Kasuga-koen, Kasuga, Fukuoka 816-8580, Japan
e-mail: hu@riam.kyushu-u.ac.jp

M. Kashiwagi
Graduate School of Engineering, Osaka University, 2-1 Yamada-oka, Suita, Osaka 565-0871, Japan

Keywords CIP method · THINC scheme · Virtual particle method · Water on deck · Strongly nonlinear wave–body interaction

1 Introduction

A Cartesian grid approach for predicting hydrodynamic loads associated with strongly nonlinear ship–wave interactions has been developed over a period of years in the Research Institute for Applied Mechanics (RIAM) at Kyushu University. The two- and three-dimensional development of the CFD code has been presented in previous papers [1, 2]. The constrained interpolation profile (CIP) algorithm [3] was adopted as the base scheme to obtain a robust flow solver for the Cartesian grid approach. The Cartesian grid used for the numerical solution does not depend on the locations of the body boundary and the free surface. The use of such a grid makes the computation of strongly nonlinear problems with complicated free-surface deformation and violent body motion more efficient and robust than conventional body-fitted approaches. We call this numerical method the "CIP-based Cartesian grid method" in this paper.

The free surface and the body boundary in the present numerical model are treated as immersed interfaces. As shown in Fig. 1, to recognize different phases we define a density function (or color function) ϕ_m, in which $m = 1, 2, 3$ denote the liquid, gas and solid phases, respectively. In each computational cell these density functions satisfy $\Sigma\phi_m = 1.0$.

The moving free surface can be captured by the numerical solution of the equation for ϕ_1. Several types of CIP-based interface capturing methods have been applied for the free surface, such as original CIP and a CIP–

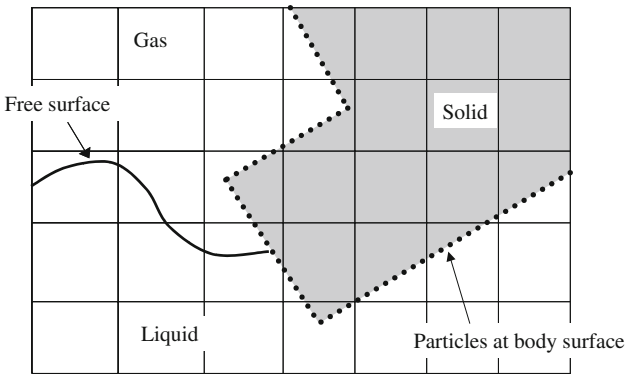

Fig. 1 Concept for the Cartesian grid approach

conservative semi-Lagrangian scheme with a third-order polynomial function (CIP–CSL3) [4]. The original CIP scheme is simple and accurate enough for many free surface problems [1]. For long computations, however, we have observed the problems of poor mass conservation and interface smearing at the free surface. To solve these problems, we have applied the CIP–CSL3 scheme, which is a conservation scheme including an antidiffusion treatment, to the numerical simulation of a violent sloshing problem [5]. It was found that the CIP–CSL3 scheme behaves better as an interface-capturing scheme than the original CIP scheme. However, the CIP–CSL3 interface-capturing scheme gives a density function variation that overshoots and undershoots at the free surface, and the scheme is complicated. In this paper, we apply a new interface-capturing scheme, the THINC scheme [6], which can overcome the drawbacks of the CIP–CLS3 scheme.

The floating body is treated as a rigid body in the present computation, and its violent motions and complicated interactions with the free surface can be solved by applying a Cartesian grid method in a relatively easy way. The penalty incurred by using an underlying Cartesian grid is its low-order accuracy near the body boundaries, because the grid lines generally do not conform to the body boundaries. In order to improve the accuracy of the calculation we have developed a virtual particle method [2]. The solid body is represented by distributing virtual particles on the surface as shown in Fig. 1. The boundary condition is satisfied at these particles. An advantage of this treatment is that the extension from two dimensions to three dimensions is straightforward. We have already carried out some three-dimensional computations using the virtual particle method [7].

One difficulty with the development of this code is the lack of available experimental data for validation. This motivated us to design a two-dimensional benchmark wave–body interaction experiment for validating numerical methods on strongly nonlinear problems. For this purpose, the experimental conditions were made as simple as possible. Both the body motion and the free surface elevation at a particular point are measured and can be easily compared to numerical simulations.

This paper is organized as follows. The Sect. 2 describes the CIP-based Cartesian grid method. First, the flow solver is briefly summarized. The THINC scheme, which is used as the interface capturing method, is then explained. In Sect. 3, the wave–body interaction experiment is described. The Sect. 4 presents the numerical results. The first example is a dam-breaking computation in a rectangular tank. Results obtained by using different interface capturing methods are compared to show the efficiency of the THINC scheme. The second and third examples are about the present experiments on forced oscillation in heave and the wave–body interaction, respectively. The paper ends with Sect. 5.

2 Numerical method

The CIP-based Cartesian grid method used for the present computations is summarized in this section. A turbulence model is not included and surface tension is neglected.

2.1 Flow solver

We consider an unsteady, viscous (laminar) and incompressible flow. The governing equations are as follows:

$$\frac{\partial u_i}{\partial x_i} = 0 \tag{1}$$

$$\frac{\partial u_i}{\partial t} + u_j \frac{\partial u_i}{\partial x_j} = -\frac{1}{\rho}\frac{\partial p}{\partial x_i} + \frac{1}{\rho}\frac{\partial}{\partial x_j}\left(2\mu S_{ij}\right) + f_i \tag{2}$$

where $S_{ij} = (\partial u_i/\partial x_j + \partial u_j/\partial x_i)/2$. The last term on the right-hand side of Eq. 2 stands for the body force, such as gravity, etc. The time evaluation of Eq. 2 is performed by a fractional step method in which the equation is divided into three calculation steps: an advection step and two non-advection steps. In the advection calculation step, the CIP scheme is applied. The pressure is treated in a non-advection calculation step, in which the following Poisson equation is used:

$$\frac{\partial}{\partial x_i}\left(\frac{1}{\rho}\frac{\partial p^{n+1}}{\partial x_i}\right) = \frac{1}{\Delta t}\frac{\partial u_i^{**}}{\partial x_i} \tag{3}$$

where the superscript "$n + 1$" stands for the new time step, and "**" for the time level just after the first non-advection calculation step. Equation 3 is assumed valid for liquid, gas and solid phases. Numerical solution of Eq. 3 gives the pressure distribution over the whole computation domain. We should note that the pressure distribution obtained inside the solid body is a fictitious one, which satisfies the

divergence-free condition of the velocity field. In such a treatment, the pressure boundary condition at the interface between different phases is not necessary, and a fast solver or parallel computing technique can easily be applied. More details about the fractional step treatment used in the flow solver can be found in the previous paper [1].

2.2 Treatment of inner interfaces

The wave–body interaction problem in the proposed numerical model is treated as a multiphase problem, which includes a liquid phase (water), a gas phase (air) and a solid phase (floating body). The interfaces between different materials need to be determined in the computation. This can be done by solving the following equation for the density function:

$$\frac{\partial \phi_m}{\partial t} + u_i \frac{\partial \phi_m}{\partial x_i} = 0 \tag{4}$$

We only need to solve two of the density functions, e.g., ϕ_1 for the liquid and ϕ_3 for the solid; we can then obtain the third one by

$$\phi_2 = 1 - \phi_1 - \phi_3 \tag{5}$$

After all of the density functions have been determined, any physical property λ, such as the density or the viscosity, can be calculated for each computation cell as follows:

$$\lambda = \sum_{m=1}^{3} \phi_m \lambda_m \tag{6}$$

The density and the viscosity of the solid body are set to be the same as those of the liquid for the purposes of numerical stability. The drawback of the averaging process of Eq. 6 is that the computational accuracy is reduced to first order in terms of cell size at the interfaces.

There are two kinds of the interface in the wave–body interaction problem: the gas–liquid interface (free surface) and the solid–fluid interface (body surface). The THINC scheme is applied to the free surface, and the virtual particle method was developed for the floating body surface. In the following, we describe these two interface treatments.

2.2.1 THINC scheme for capturing the free surface

The THINC scheme was proposed by Xiao et al. [6] for incompressible free surface flow. Some test examples indicated that the scheme has the features we need for our computations: mass conservation and a lack of oscillation and smearing at the interface. A 1-D THINC scheme is described in the following. Multidimensional computations are performed by a dimensional splitting method [8].

The one-dimensional advection equation for a density function ϕ can be written in conservation form as follows:

$$\frac{\partial \phi}{\partial t} + \frac{\partial (u\phi)}{\partial x} = \phi \frac{\partial u}{\partial x} \tag{7}$$

Equation 7 is discretized by a finite volume method. For a known velocity field u^n, integrating Eq. 7 over a computational cell $[x_{i-1/2}, x_{i+1/2}]$ and a time interval $[t^n, t^{n+1}]$ yields:

$$\bar{\phi}_i^{n+1} = \bar{\phi}_i^n - \frac{1}{\Delta x_i}\left(g_{i+1/2} - g_{i-1/2}\right) + \frac{\Delta t}{\Delta x_i}\bar{\phi}_i^n\left(u_{i+1/2}^n - u_{i-1/2}^n\right) \tag{8}$$

where $\Delta x_i = x_{i+1/2} - x_{i-1/2}$, $\Delta t = t^{n+1} - t^n$, $\bar{\phi}_i = \int_{x_{i-1/2}}^{x_{i+1/2}} \phi \mathrm{d}x$ is the cell-averaged density function defined at the cell center ($x = x_i$), and $g_{i\pm\frac{1}{2}} = \int_{t^n}^{t^{n+1}} (u\phi)_{i\pm\frac{1}{2}} \mathrm{d}t$ is the flux across the cell boundary ($x = x_{i\pm1/2}$). The third term on the right hand side of (7) is an approximate expression. The fluxes are calculated by a semi-Lagrangian method. Similar to the CIP scheme, the profile of ϕ inside an upwind computation cell is approximated by an interpolation function. Instead of using a polynomial in the CIP scheme, the THINC scheme uses a hyperbolic tangent function in order to avoid numerical smearing and oscillation at the interface. Since $0 \le \phi \le 1$, and the variation of ϕ across the free surface is step-like, a piecewise modified hyperbolic tangent function is used to approximate the profile inside a computation cell, which is shown as follows:

$$F_i(x) = \frac{\alpha}{2}\left\{1 + \gamma \tanh\left[\beta\left(\frac{x - x_{i-1/2}}{\Delta x_i} - \delta\right)\right]\right\} \tag{9}$$

where α, β, γ, δ are parameters to be specified. α and γ are parameters used to avoid interface smearing, which are given as follows:

$$\alpha = \begin{cases} \bar{\phi}_{i+1} & \text{if } \bar{\phi}_{i+1} \ge \bar{\phi}_{i-1} \\ \bar{\phi}_{i-1} & \text{otherwise} \end{cases} \qquad \gamma = \begin{cases} 1 & \text{if } \bar{\phi}_{i+1} \ge \bar{\phi}_{i-1} \\ -1 & \text{otherwise} \end{cases} \tag{10}$$

Parameter β is used to control the sharpness of the variation of the function, and its effect is shown in the Sect. 4.1 by a test computation. Parameter δ is used to determine the middle point of the hyperbolic tangent function, and is calculated by solving the following equation:

$$\frac{1}{\Delta x_i}\int_{x_{i-1/2}}^{x_{i+1/2}} F_i(x)\mathrm{d}x = \bar{\phi}_i^n \tag{11}$$

After $F_i(x)$ is determined, the flux at the cell boundary can be calculated by Eq. 9. In Fig. 2, $g_{i+1/2}$ for $u_{i+1/2} \ge 0$ is indicated by the dashed area. After all of the fluxes across the cell boundaries have been calculated, the cell-integrated

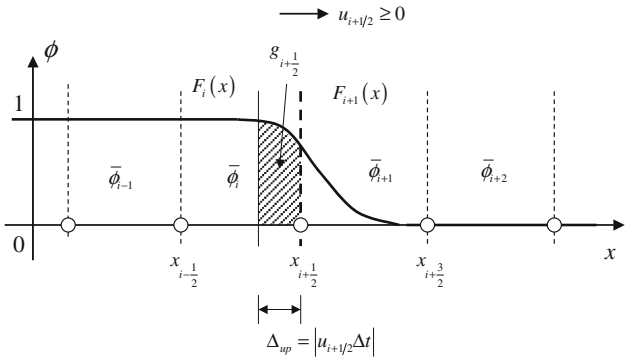

Fig. 2 Concept of the THINC scheme

value at the new time step $\bar{\phi}_i^{n+1}$ can be obtained by Eq. 8. This cell-integrated value is used to determine the free surface position; therefore, mass conservation is automatically satisfied for the liquid.

2.2.2 *Virtual particle method for the floating body*

The floating body is considered a rigid body. To calculate the fluid–body interaction in a Cartesian grid, we need to solve some problems. The first problem is how to calculate the density function for the solid phase ϕ_3 in each computation cell when the body moves in a stationary Cartesian grid. The velocity for a solid cell ($\phi_3 = 1$), which is denoted by $\hat{U}_i^{n+1}$, can be calculated from the motion equations of the rigid body. However, the boundary cell ($0 < \phi_3 < 1$) must be treated. If ϕ_3 is known, the effect of the solid body on the surrounding flows can be considered by the following updating procedure after the computation of Eq. 2:

$$U_i^{n+1} = \phi_3 \hat{U}_i^{n+1} + (1 - \phi_3) u_i^{**} \tag{12}$$

where u_i^{**} is the velocity from the computation of Eq. 2. Equation 12 is a volume-fraction weighting treatment for velocity interpolation in a boundary cell. Such treatment where the velocity distribution inside the body and the body surface is imposed is equivalent to applying a forcing term to the momentum equation. The second problem is how to determine the solid body velocity $\hat{U}_i^{n+1}$at the boundary cell.

The above-mentioned two problems for rigid body calculations can be solved by a virtual particle method that we have developed. As shown in Fig. 1, the particles are distributed on the body surface. After the hydrodynamic forces on the body are obtained, it is not difficult to calculate the translational and rotational velocities at the gravitational center of the rigid body. Then, for all particles, we can obtain the position, the normal unit vector and the velocity for the new time step. The density function ϕ_3 for a computational cell can easily be calculated in an approximate manner using the positions and the normal vectors of all particles in the cell. The velocity at the body boundary cell $\hat{U}_i^{n+1}$, which must be specified as a boundary condition, can be calculated by interpolation using the velocities of the particles.

3 Experimental investigation

The experiment was carried out in a two-dimensional wave channel (10 m long, 0.3 m wide and 0.4 m deep) at RIAM, Kyushu University. As shown in Fig. 3, the floating body model for the experiment was a box-type with a breadth of $B = 0.5$ m, a depth of $D = 0.10$ m and a freeboard of $f = 0.025$ m. A box-type superstructure was installed on the deck. The length of the body was $L = 0.29$ m, and the clearance between the body and the tank sidewall was $c = 5$ mm. Regular waves were generated by a plunger-type wave-maker. An active wave-absorbing device was installed at the downstream end.

3.1 Forced oscillation test in heave

A forced oscillation test in heave was carried out with the floating body model. We found from the experiment that the three-dimensional effect could influence the results for high frequencies. Figure 4 shows a comparison of the added-mass and damping coefficients for two experiments with different clearances with the results from a boundary element method (BEM) computation based on linear potential theory. The BEM program was developed by one of the authors. The clearances between the body and the tank sidewall for the two experiments were $c = 5$ mm and $c = 1$ mm, respectively. The nondimensional frequency is defined as $Ka = 0.5\omega^2 B/g$, where g is the acceleration due to gravity. The experimental results for $c = 5$ mm show a strange tendency when $Ka \geq 1.5$, which cannot be explained by viscous effects alone. The three-dimensional effect is considered important for high-frequency oscillation, because the results for $c = 1$ mm, which is considered to show less of a three-dimensional effect, show a reasonable agreement with the BEM results. The experimental results for $c = 1$ mm were used to validate the two-dimensional hydrodynamic force calculations.

In order to obtain information on the quality of the experiment, an uncertainty analysis was carried out on the measured data from the forced oscillation test. Except for the three-dimensional effect, the sources of error in the experiment may include those arising from the measuring devices and calibration. Since it is not possible to quantify these errors in the experiment, the experimental uncertainty was investigated by checking the level of dispersion of the data. For this purpose, one test run, a forced oscillation test

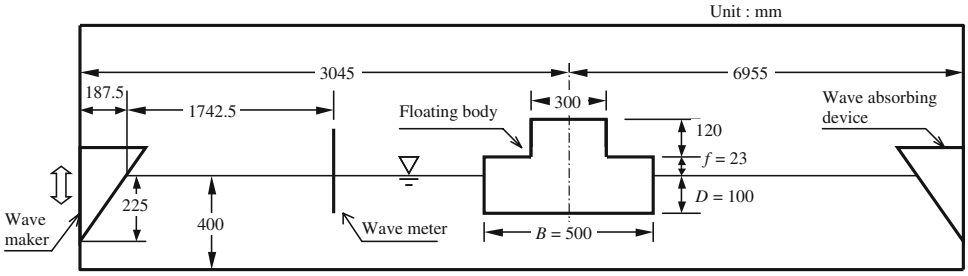

Fig. 3 Schematic view of the two-dimensional wave–body interaction experiment

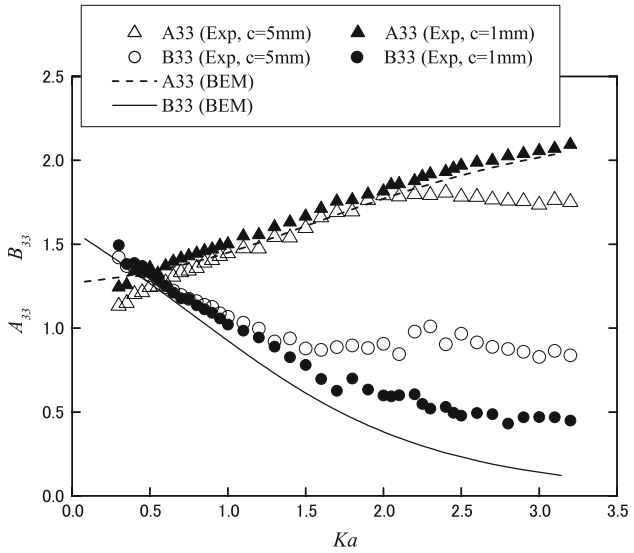

Fig. 4 Comparison of the added-mass and damping coefficients for two experiments ($c = 5$ mm and $c = 1$ mm) with the results from a BEM computation

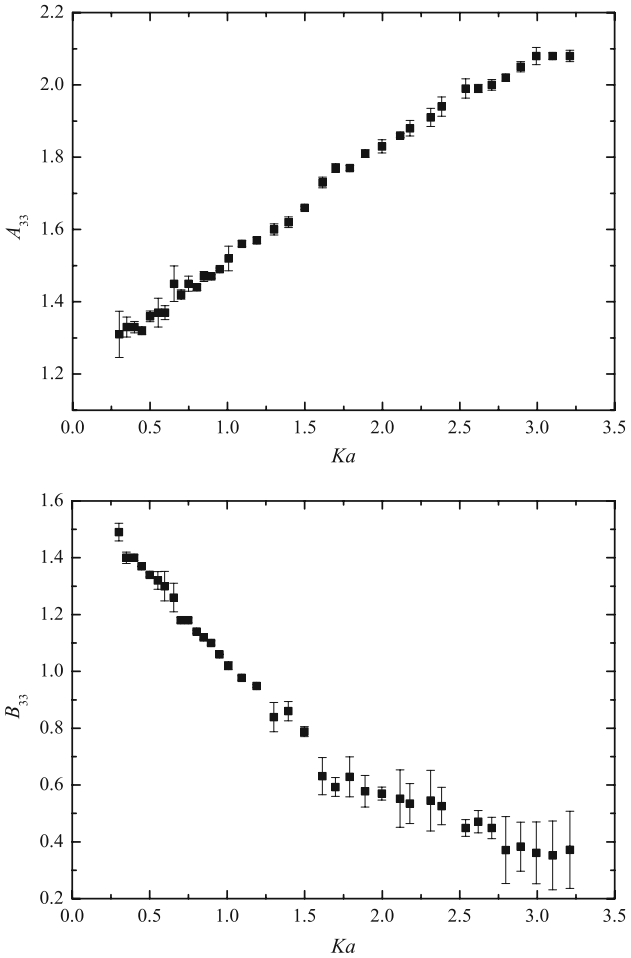

Fig. 5 Repeated tests of added-mass and damping coefficients. The *square dot* denotes the averaged value, and the *error bar* denotes the range of the data

with an amplitude of $Y = 0.01$ m, was repeated five times. The results for the averaged value and the scatter in the added-mass and damping coefficients are shown in Fig. 5. The repeated tests gave good agreement in terms of the added-mass coefficient. For the damping coefficient, however, the dispersion increased with Ka. When $Ka > 2.0$, the scatter in the data was high. Part of the reason for this is the fact that the damping force is relatively small in high-frequency oscillation; therefore, measurements of it are easily affected by the errors associated with the measuring devices.

3.2 Wave–body interaction test

In the wave–body interaction tests, the model was free to heave, sway and roll. The clearance between the body and the tank sidewall was set to $c = 5$ mm because we needed to guarantee that there was no interference between the body and the tank sidewall in the experiment. As the frequency Ka considered in the experiment was less than 1.5, we considered that this clearance was acceptable according to the above discussion on the forced oscillation test.

Another point that should be mentioned here is that the wave-absorbing function of the wave-maker was not switched on. This means wave reflection may occur on the wave-maker side. On the downstream side, a wave-absorbing apparatus was used to damp the outgoing waves. No obvious wave reflection at the downstream end was observed at the studied frequencies.

In the experiment, we measured the displacement of the wave-maker, the motion (heave, roll and sway) of the floating body, and the wave elevation at the point between

the wave-maker and the floating body. The record of the motion of the wave-maker is used as input data in the computation. Other measurements are compared with the numerical results. In the experiment, the heave motion and the roll motion of the floating body were free, while its sway motion was either fixed (fixed-sway case) or restrained by a spring with a spring constant of 7.6 N/m^2 (free-sway case).

In the experiment, three amplitudes of $Y = 5$, 15, 25 mm and 12 periods ranging from 0.70 to 1.30 s were considered for the wave-maker motion.

4 Numerical results

Three two-dimensional computations are presented in this section to evaluate the performance of the proposed numerical method. The first example is a dam-breaking problem taken from a previous study performed by the authors [1]. The behavior of the THINC scheme as an interface-capturing method is investigated. The second example is a forced oscillation test in heave with the rectangular floating body. The hydrodynamic force coefficients are compared to those from the experiment described in the previous section. The third computation focuses on the wave–body interaction experiments described in the previous section. Both the fixed-sway and free-sway cases are considered.

For all of the computations, the effects of both the grid spacing and the time step were carefully investigated, and the values showing in the following are considered reasonable choices.

4.1 Dam-breaking problem

The dam-breaking problem is illustrated in Fig. 6. In the computation, a variable grid was used, in which the grid points were concentrated near the floor and the right wall. The grid number was 240 × 96, and the minimum grid spacing was 5 mm. The time step was set to $\Delta t = 10^{-4}$ s.

Two interface capturing methods, THINC and CIP, were used, and the results for the free-surface variations are compared in Fig. 7. The free surface is indicated by density function contours, with the three lines showing $\phi = 0.05$, 0.5 and 0.95. The solid line is $\phi = 0.5$. The distance between the two dashed lines roughly represents the transient distance from liquid to gas; in a physical problem this thickness should be zero. The free surfaces computed by the THINC scheme are very compact; the thickness of the computed free surface (the distance between $\phi = 0.05$ and 0.95) is two to three times the size of the cell. On the other hand, those obtained by the CIP scheme are diffusive after the overturning water hits the free surface.

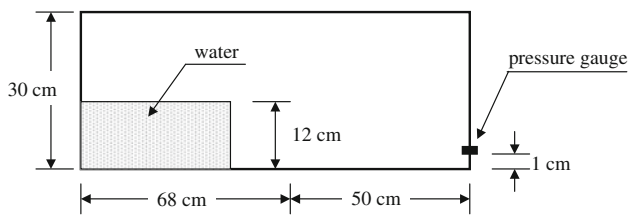

Fig. 6 Schematic view of the dam-breaking problem

There is only one parameter to be determined in the THINC scheme, the parameter β. Xiao et al. [6] suggested that $\beta = 3.5$ is a good choice based on some numerical tests, and this value was also used in the computation shown in Fig. 7. To check the influence of β, we show three results for density function contours in Fig. 8, where $\beta = 2.0$, 3.5, 5.0 are used, respectively. An obvious trend is that a larger β results in a more compact free surface. However, the computed free surface may become wrinkled when β is too large, e.g., $\beta = 5.0$. It is apparent from Fig. 8 that although the compactness of the computed free surface is not very sensitive to β, $\beta = 3.5$ seems to be a reasonable choice.

In Fig. 9, we compare the computed time series for the pressure at point A to that observed experimentally. The computations were performed using two interface-capturing methods. The two peaks in the pressure over time correspond to the times when the water hits the vertical wall and the overturning water hits the free surface, respectively. All of the computations predict the pressure before the second peak accurately. After the second peak, the free surface becomes fully three-dimensional, and the two-dimensional computations overpredict the pressure. The results from applying the CIP scheme show some undulations that do not appear in the experiment.

Finally, we checked the conservation of water mass for the computations. Figure 10 shows the variation in the total water mass in the tank over time. Variations of up to ±0.5% were found for the CIP scheme, while the variation in total mass for the THINC scheme was below 10^{-9}%—the conservation was perfect.

4.2 Forced oscillation in still water

The computation corresponded to the forced oscillation test in still water. The floating body was forced to oscillate harmonically in heave, with motion defined by $y_f(t) = Y \sin(\omega t)$. Here, $\omega = 2\pi/T_f$ was defined and T_f was the period of the oscillation. Under the assumption of linearity, we write the vertical hydrodynamic force on the body as

$$F_3 = -A_{33}^* \frac{\mathrm{d}^2 y_f}{\mathrm{d}t^2} - B_{33}^* \frac{\mathrm{d}y_f}{\mathrm{d}t} - C_{33}^* y_f \tag{13}$$

where A_{33}^*, B_{33}^* and C_{33}^* are the added-mass, damping and restoring coefficients in heave, respectively. The

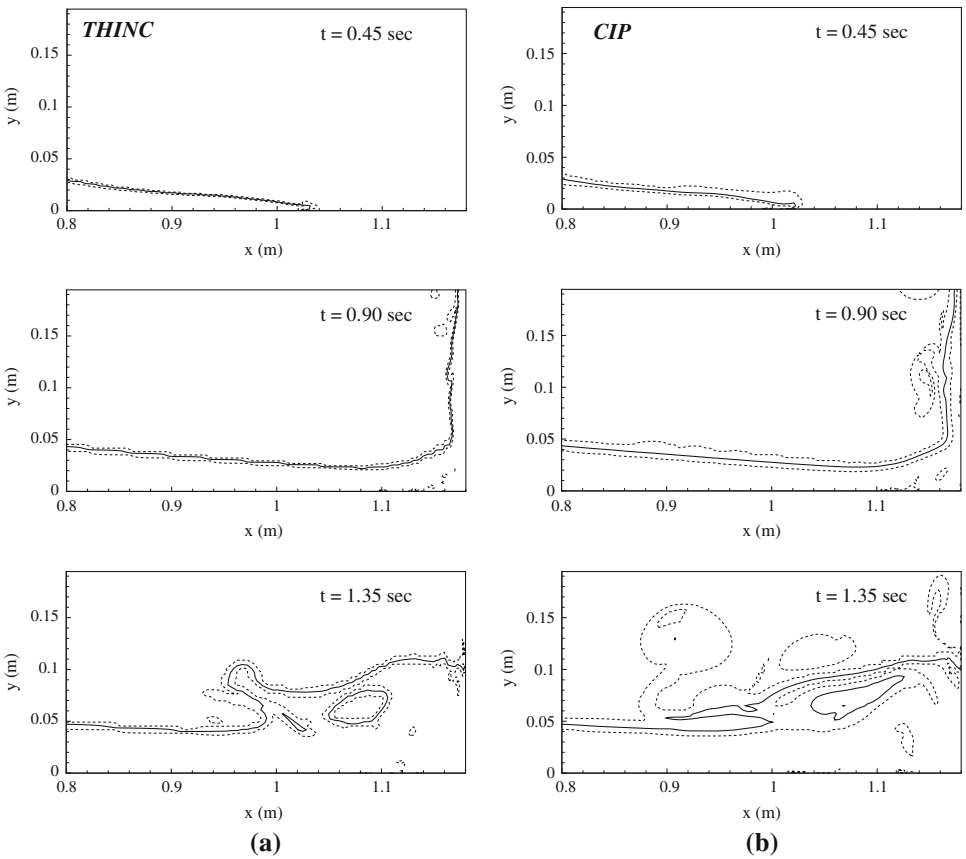

Fig. 7 Comparison of density function contours. The *three lines* indicate $\phi_1 = 0.05, 0.50, 0.95$. The interface-capturing scheme is THINC in **a** and CIP in **b**

nondimensional added-mass and damping coefficients are defined as $A_{33} = A^*_{33}/\rho a^2$ and $B_{33} = B^*_{33}/\left(\rho a^2\sqrt{g/a}\right)$, respectively. Here, $a = B/2$ is the half-breadth.

In the computation, the effects of both the grid spacing and the time step were carefully investigated. Table 1 shows a grid resolution test for the case of $Ka = 1.8$ and $Y = 0.01$ m. Four grids with the number of grid points varying from 154×54 to 630×284 were considered. The grid spacing was variable for each grid in order to concentrate the grid point onto the floating body. The results for A_{33} and B_{33} were affected by the grid resolution; however, it was found that convergence can be achieved for Grids 3 and 4. Therefore, the resolution of Grid 3 was considered sufficient for the studied problem and was adopted for the computation shown below. On the other hand, the time step did not affect the results so long as the Courant number in terms of maximum flow velocity was kept to <0.5 in the computation. This restriction on the time step was used in all of the computations.

In Figs. 11 and 12, comparisons of the added-mass and damping coefficients are shown. A grid of $500(x) \times 183(y)$ was used with a minimum grid spacing of $\Delta x = \Delta y = 3$ mm around the body. The time step was $\Delta t/T_f = 10^{-3}$. The total simulation time was $15T_f$, and the results obtained after $10T_f$ were used to calculate the force coefficients. The oscillation amplitudes were $Y = 5$, 10 mm. BEM results for potential flow are also plotted in the two figures. Comparisons of the added-mass coefficients between the experiment and the computations for both viscous flow and potential flow indicate good agreement. For the damping coefficients, the results from the experiment and the present CIP computation agree well with each other, while the potential flow results obtained by BEM are lower for $Ka > 1.5$. The reason for this is that the BEM computation neglects viscous effects. For the present body shape and scale, damping due to vortex shedding should also be important. Vortex shedding can be seen in the CIP computation shown in Fig. 13, which is a snapshot of the velocity field at $t/T_f = 10$ for $Ka = 1.5$.

We can estimate the damping coefficient due to the vortex shedding in an approximate way. If we do not consider the effect of the free surface, the drag force on the floating body due to the vortex shedding can be approximated by the following formula for a square cylinder:

$$F_D = \frac{1}{4} C_D B \rho \left|\dot{y}_f\right| \dot{y}_f \tag{14}$$

where the constant 1/4 is used instead of 1/2 because the floating body is considered a half-cylinder. The drag coefficient C_D is dependent on the KC number, which can be defined as follows for the floating body:

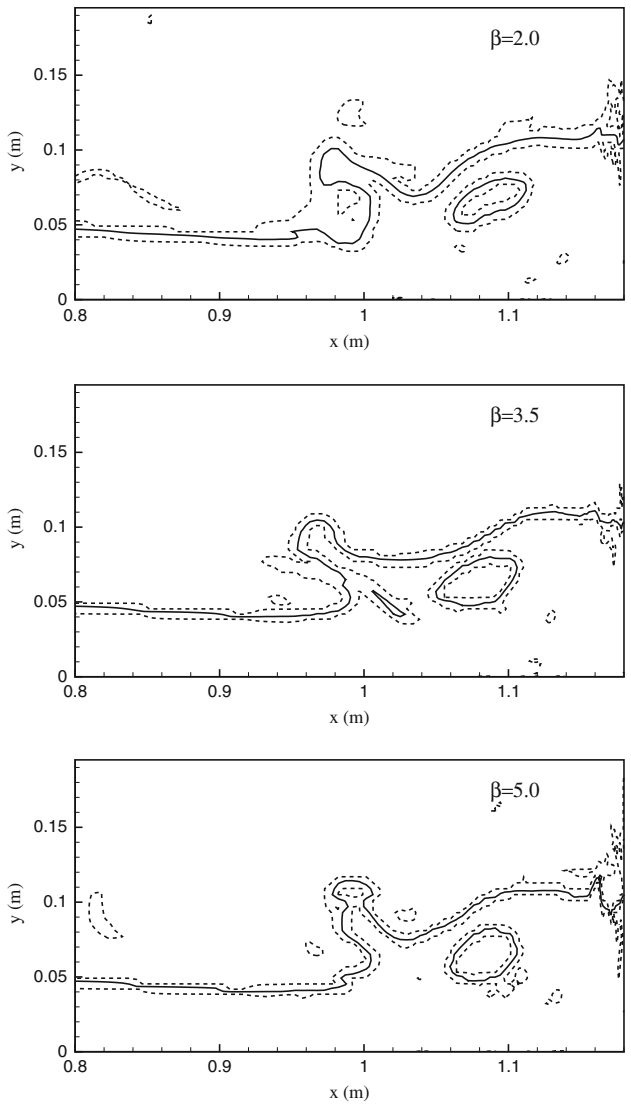

Fig. 8 Density function contours computed by using THINC to show the effect of the parameter β; the *three lines* indicate $\phi_1 = 0.05, 0.50, 0.95$

$$\mathrm{KC} = \frac{2\pi Y}{B} \tag{15}$$

In this experiment, KC = 0.0628 and 0.127 correspond to Y = 5 and 10 mm, respectively. No experimental results are available for such a small KC number. From the experiment by Vengatesan et al. [9], drag coefficients of $C_{\mathrm{D}} = 25$ and 20 might be reasonable estimates for the floating body at KC = 0.0628 and 0.127, respectively.

Let ${B_{33}}^{D}$ be the damping coefficient due to the vortex shedding. Then we write the viscous damping force as

$$F'_D = B^D_{33}\rho a^2\sqrt{g/a}\,\dot{y}_f \tag{16}$$

By assuming that the work over one oscillation period for F'_D and F_D is the same, i.e., $\int_0^T F'_D\dot{y}_f \mathrm{d}t = \int_0^T F_D\dot{y}_f \mathrm{d}t$, we obtain

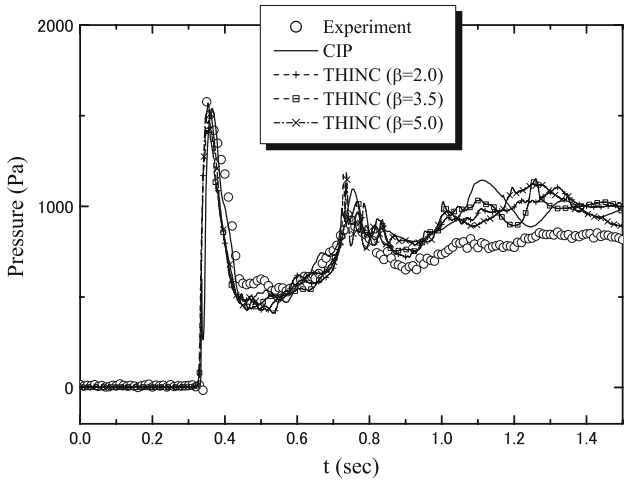

Fig. 9 Comparison of the pressure at the wall obtained computationally with that observed experimentally

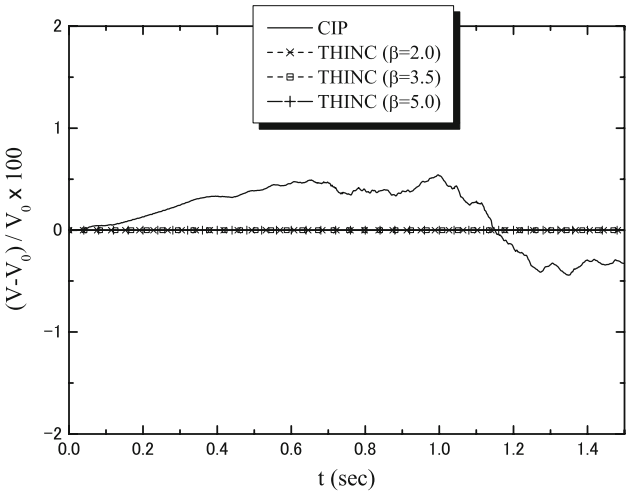

Fig. 10 Conservation of liquid mass for different interface-capturing schemes

$$B^D_{33} = \frac{4C_{\mathrm{D}}Y}{3\pi a}\sqrt{Ka} \tag{17}$$

The viscous damping by Eq. 17 is added to the BEM result and is shown in Fig. 12 by a dashed line. It can be seen that the effect of the vortex shedding could be a reasonable explanation for the underestimated damping coefficients obtained when using the BEM method.

4.3 Wave–body interaction

To check the general motion features of such floating body in waves, a computation based on linear potential flow theory was first carried out for the fixed-sway case. The results are shown in Figs. 14 and 15 for amplitude and phase, respectively. The resonant period for roll is $T_{\mathrm{r}} \approx 0.9$ s. In the experiment, the wave periods cover this

Table 1 Results from a grid convergence test for forced oscillation computation ($Ka = 1.8$, $Y = 0.01$ m)

Grid no.	1	2	3	4	Experiment
Number of points	154 × 54	250 × 92	500 × 184	630 × 284	
Minimum grid spacing	0.01 m	0.006 m	0.003 m	0.002 m	
A_{33}	2.056	1.812	1.762	1.770	1.764
B_{33}	0.625	0.643	0.664	0.663	0.699

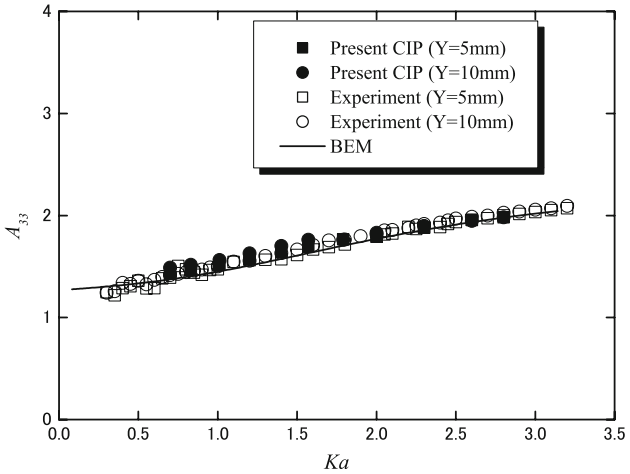

Fig. 11 Comparison of the added-mass coefficients in heave

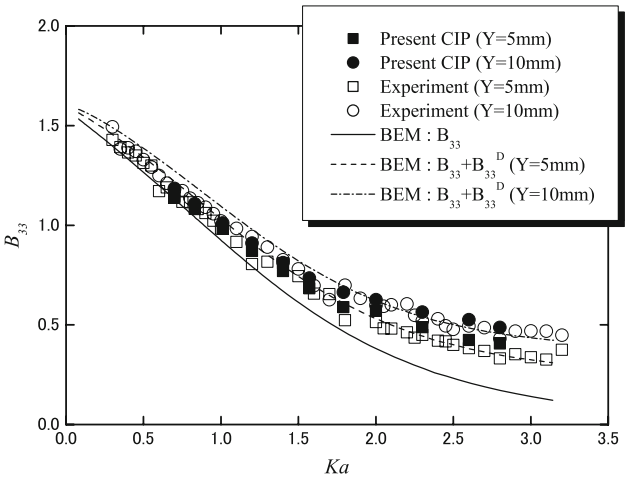

Fig. 12 Comparison of the damping coefficients in heave

resonant point. Due to the small freeboard, water on deck is observed for small wave period cases ($T_w < T_r$). This is explained by Fig. 15, where for $T_w < T_r$, the body motion tends to be out of phase with the free surface. When $T_w > T_r$, the body motion tends to be in phase with the free surface, and no water on deck occurs. It was also found from the experiment that when water moved onto the deck, the motion of the body showed strongly nonlinear behavior. In this section, we chose two typical wave periods for

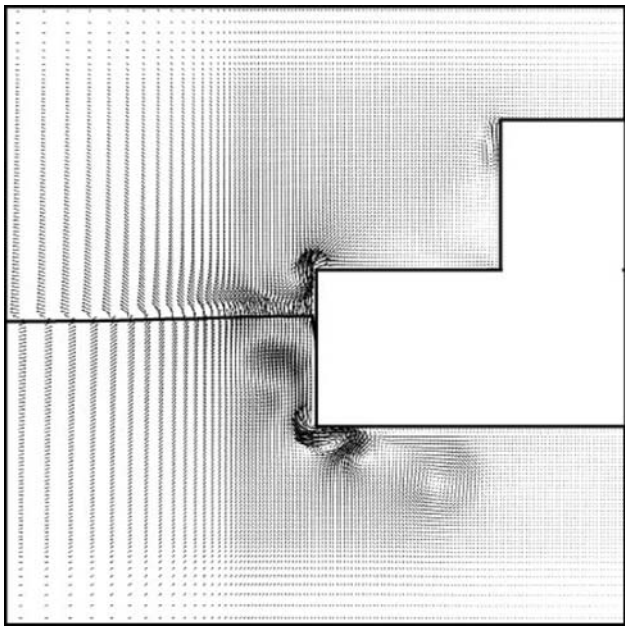

Fig. 13 Computed velocity vectors showing vortex shedding from the corner of the body

numerical simulation by the proposed CIP-based Cartesian grid method. The periods, $T_w = 0.7$ and $T_w = 1.0$ s, correspond to the cases with and without water on deck, respectively.

A two-dimensional numerical wave tank (NWT) was considered for the numerical simulation by the CIP-based Cartesian grid method. The computational domain was the same as shown in Fig. 3, in which the upper domain boundary was set 0.6 m from the still free surface. On the downstream vertical boundary, a damping zone was used [1].

In the computation, a stationary Cartesian grid was used with a grid number of $525(x) \times 183(y)$ and a minimum grid spacing of $\Delta x = \Delta y = 3$ mm around the body and the wave maker. The time step was set to $\Delta t/T_w = 10^{-3}$, where T_w is the wave period. Extensive comparison computations were carried out. Among them, four typical results are described in this section. The first two are fixed-sway cases and the other two are free-sway cases. By free sway we mean the floating body is restrained by a spring horizontally.

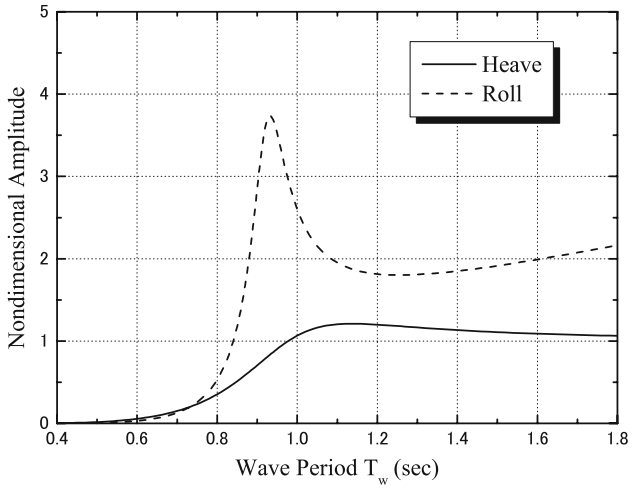

Fig. 14 Motion amplitudes computed by the potential flow theory for the fixed-sway case

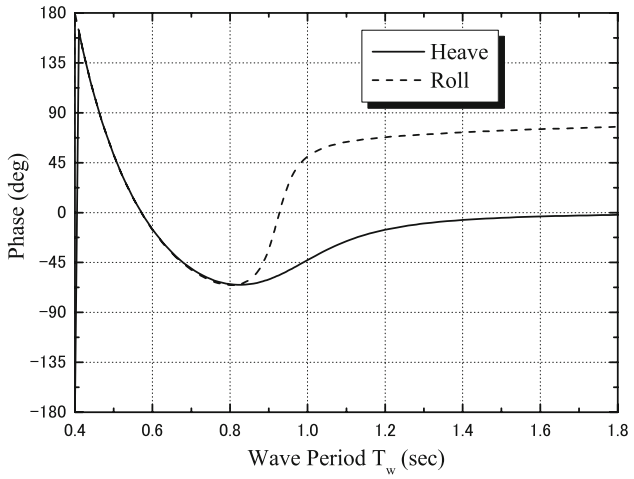

Fig. 15 Motion phases computed by the potential flow theory for the fixed-sway case

In the computations, the motion of the wave-maker was the only input data, which is taken from the experiment. The amplitude of the wave-maker motion was 25 mm and the periods were 1.0 and 0.7 s.

4.3.1 Fixed-sway case

Figures 16 17, 18 and 19 are comparisons between the results of the computation and the experiment for the fixed-sway cases. For the case of $T_w = 1.0$ s, the free surfaces computed for one period are compared in Fig. 16 with the experimental images. No water on deck phenomenon was observed. The motions of the floating body and the free surface elevation are compared in Fig. 17. The agreement between the results of the computation and the experiment was very good, and both the body motions and the free surface elevation show regular responses.

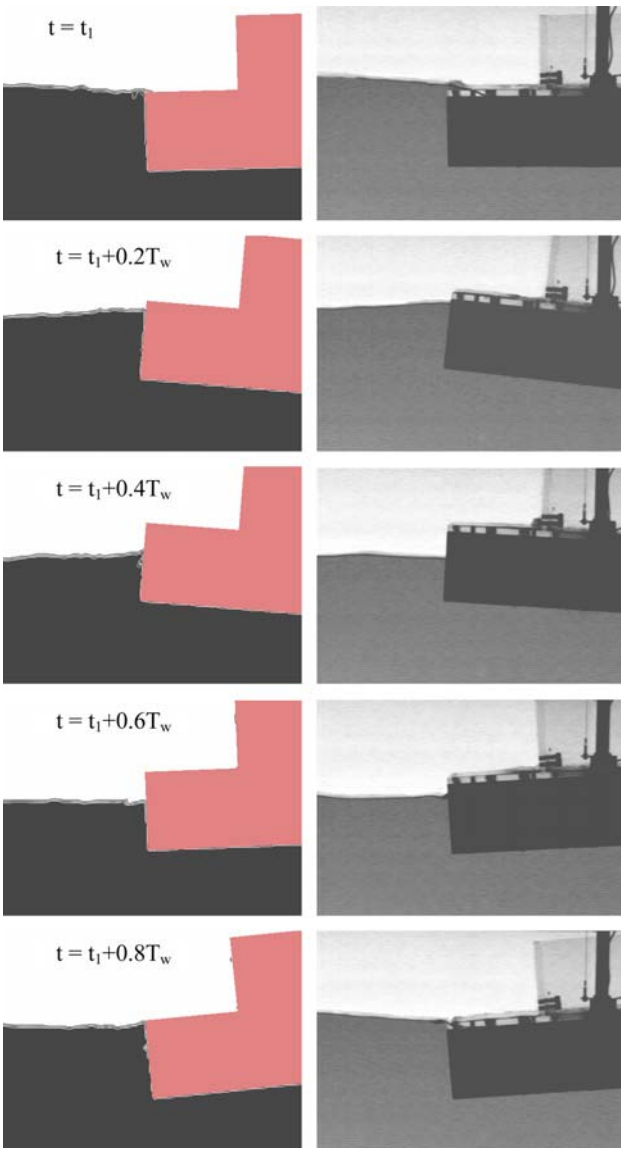

Fig. 16 Comparison of free surfaces for the case of $T_w = 1.0$ s, fixed sway

The results for $T_w = 0.7$ s are shown in Figs. 18 and 19. From the free surface variation shown in Fig. 18, we can see that the wave moves onto the deck of the floating body, strikes the superstructure, and flushes down, with some water remaining on the deck. This green water influences the motion of the body, as can be seen in Fig. 19 for the comparison between the results from the computation and the experiment. Nonlinear features appear in both the body motions and the free surface elevation. It would be interesting to see how the shipped water influences the motion of the floating body. An approximate analysis is made as follows.

We define the green water as the shaded area shown in Fig. 20. In the wave–body interaction computation, the weight W_G and the position of the center of gravity (x_{CG},

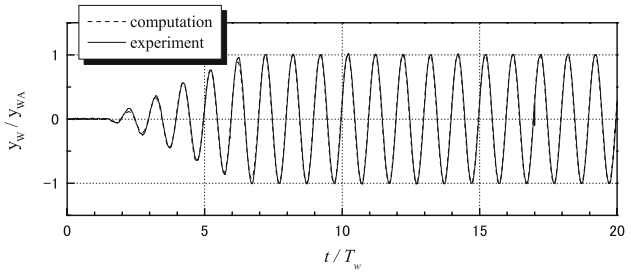

(a) wave maker motion

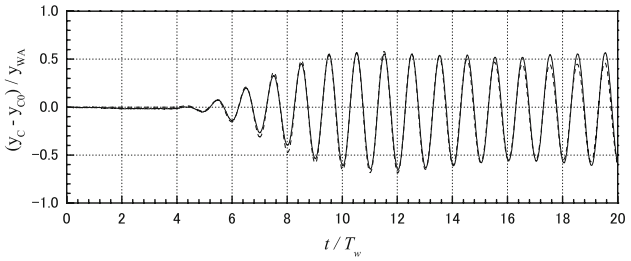

(b) heave

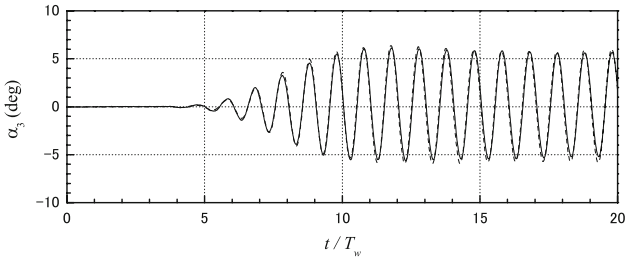

(c) roll

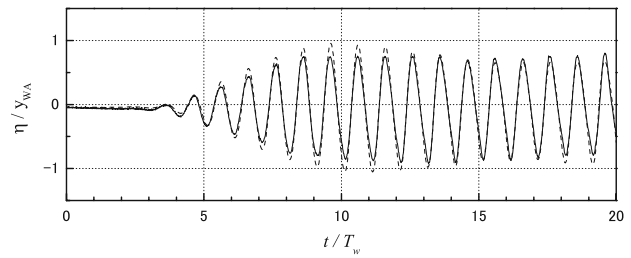

(d) wave elevation

Fig. 17 Comparison of the time histories for $T_w = 1.0$ s, fixed sway

y_{CG}) for the green water can be calculated, and the results for $T_w = 0.7$ are shown in Figs. 21 and 22, respectively. In those figures, $W_0 = 490$ N/m is the weight of the floating body, and (x_C, y_C) denotes its gravitational center. For the green water, average values of $\bar{W}_G = 10.29$ N/m, $\bar{x}_{CG} - x_G = -0.0976$ m and $\bar{y}_{CG} - y_C = 0.02917$ m, are calculated from the data between $t/T_w = 20$ and 25. Then the average heave and average roll can be obtained by static analysis of the green water effect. We have:

$$\Delta y_C^G = -\frac{W_G}{\rho g B} \tag{18}$$

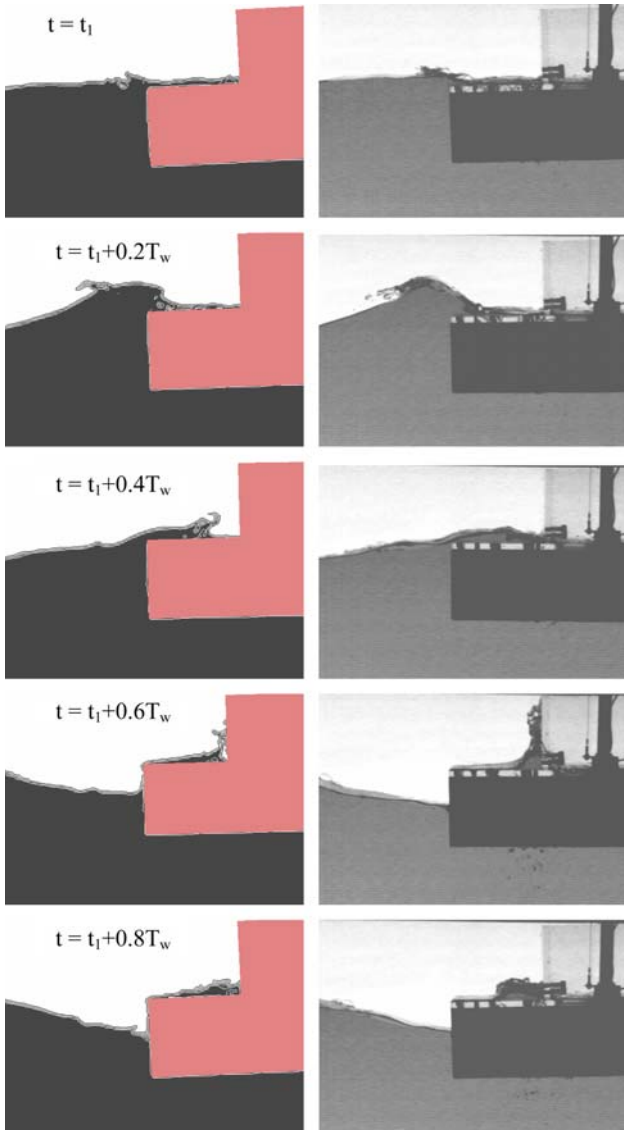

Fig. 18 Comparison of free surfaces for the case of $T_w = 0.70$ s, fixed sway

$$\Delta\alpha_3^G = \sin^{-1}\left(-\frac{W_G(x_{CG} - x_C)}{\rho g B^3/6 + W_0\overline{O'C}}\right) \tag{19}$$

The values computed for the case discussed here are $\Delta y_C{}^G = -2.1$ mm and $\Delta\alpha_3^G = 0.874°$. From Fig. 19, we can also obtain the average heave and roll as $\Delta y_C = -3.47$ mm and $\Delta\alpha_3{}^G = 1.99°$. Therefore, for the heave motion, the static effect of greenwater mass causes most of the nonlinear response. However, for the roll motion, the dynamic effect seems to be important.

4.3.2 Free-sway case

In Figs. 23 and 24, comparisons are shown for the free-sway case. The sway motion was restrained by a spring

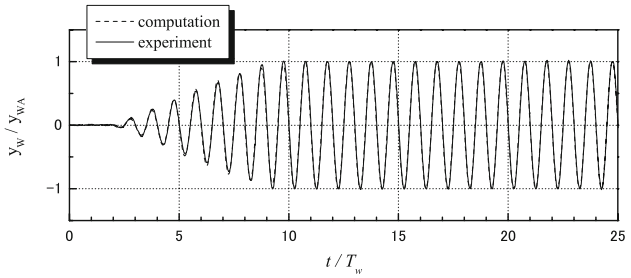

(a) wave maker motion

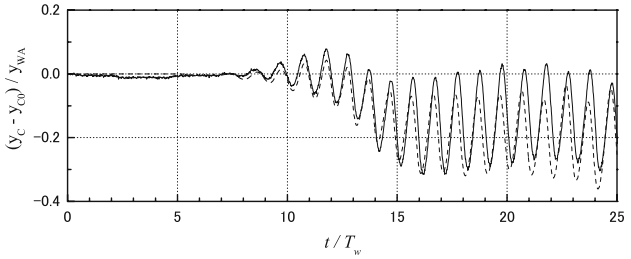

(b) heave

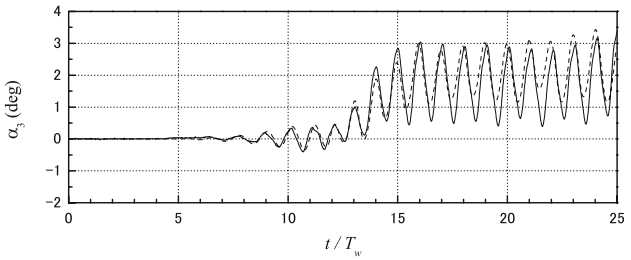

(c) roll

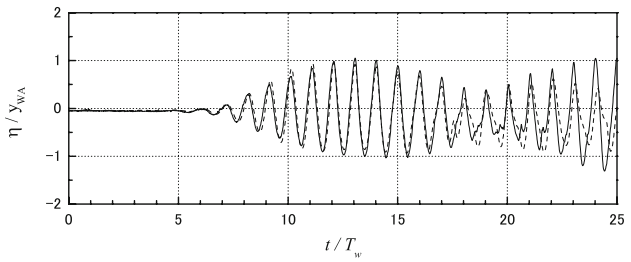

(d) wave elevation

Fig. 19 Comparison of the time histories for $T_w = 0.70$ s, fixed sway

with a spring constant of 7.6 N/m^2, and we see a large horizontal displacement of the floating body in the results from both the experiment and the computation. The results for heave, roll and wave elevation are very similar to those obtained in the fixed-sway case in Figs. 19 and 21. Disagreements are observed for the sway motion: the computed sway displacement is larger than the experimental value, especially for the case of $T_w = 1.0$ s. One possible reason for this disagreement is that mechanical friction effects have been neglected which are present in the experiment. Therefore, we introduce a damping force term into the equation for sway motion as follows:

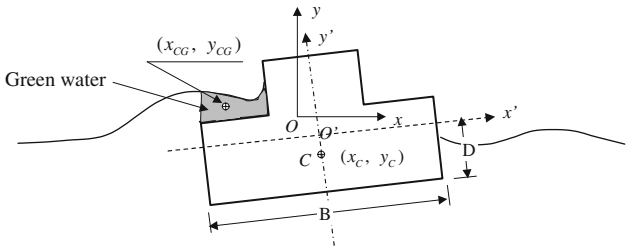

Fig. 20 Definition of the green water

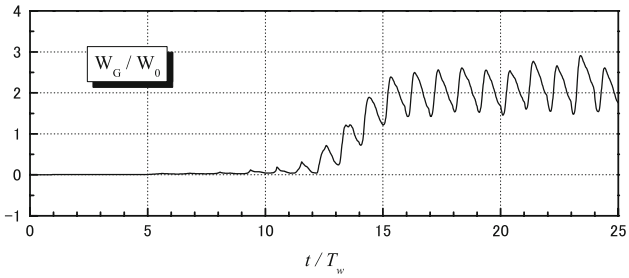

Fig. 21 Weight of the green water

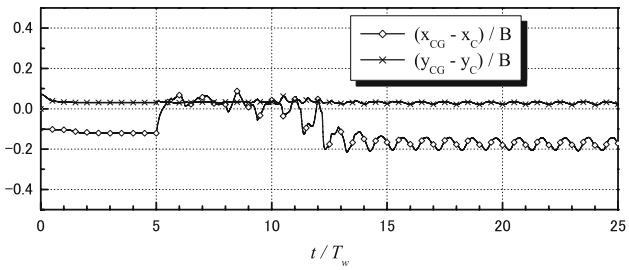

Fig. 22 Position of the green water

$$M\frac{\mathrm{d}^2 x_C}{\mathrm{d}t^2} = F_x + F_{xf} \tag{20}$$

where M is the mass of the moving system including the body and the supporting mechanism, F_x is the horizontal hydrodynamic force acting on the body, and F_{xf} is the damping force due to mechanical friction. We allow F_{xf} to be proportional to the vertical force F_z acting on the floating body and write

$$F_{xf} = -C_f |F_z| \mathrm{sign}(u_C) \tag{21}$$

where u_C is the horizontal velocity at the gravitational center of the body. It is necessary to find a suitable value for the frictional coefficient C_f. Through some test calculations, we found that $C_f = 0.13$ is good for the problems discussed here. However, the correct C_f should be determined by experiment, although this is difficult if the present experimental setup is used.

Figures 25 and 26 show the computed results for sway when mechanical friction is considered. It is apparent that

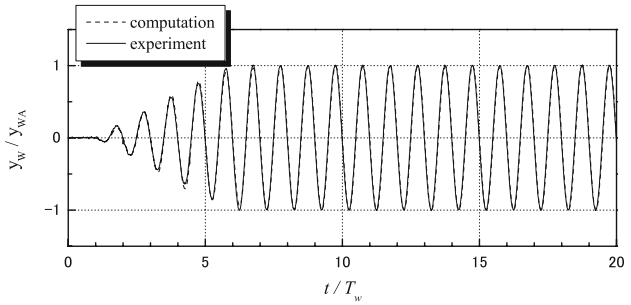

(a) wave maker motion

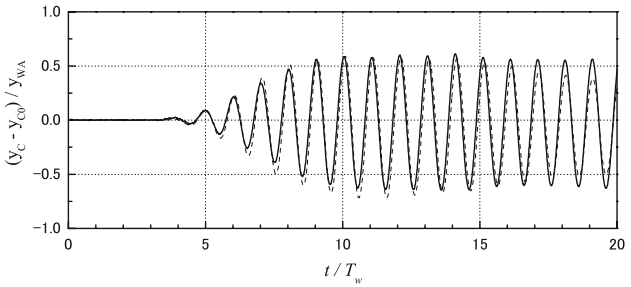

(b) heave

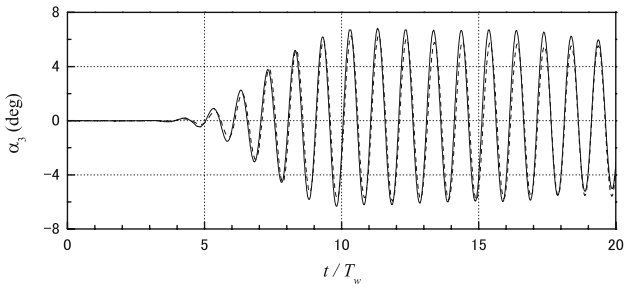

(c) roll

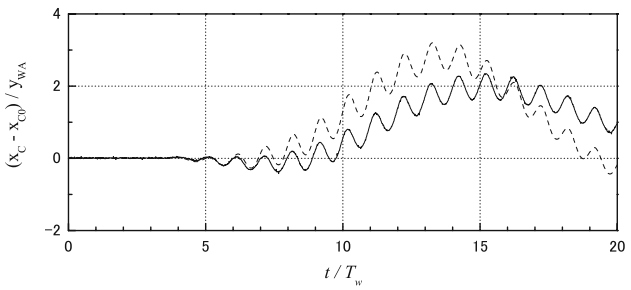

(d) sway

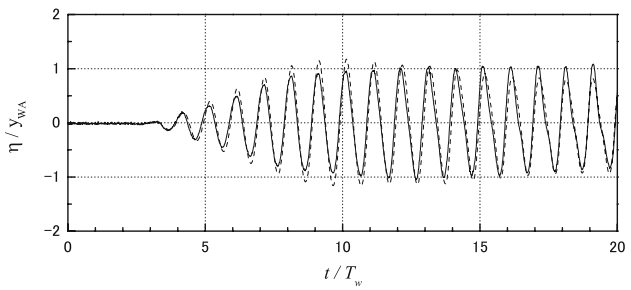

(e) wave elevation

Fig. 23 Comparison of the time histories for $T_w = 1.0$ s, free sway

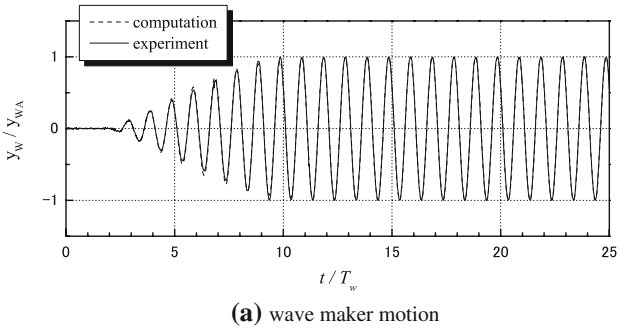

(a) wave maker motion

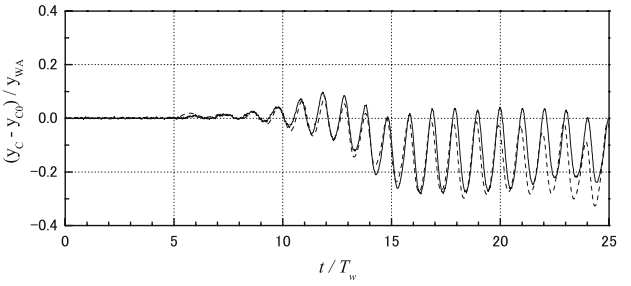

(b) heave

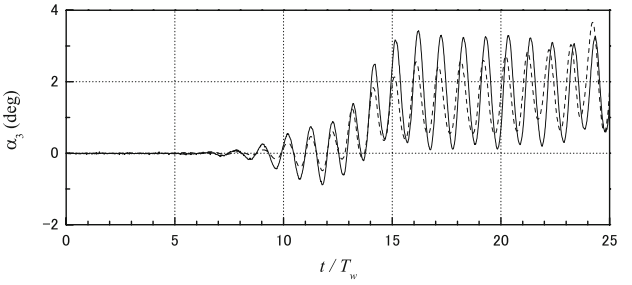

(c) roll

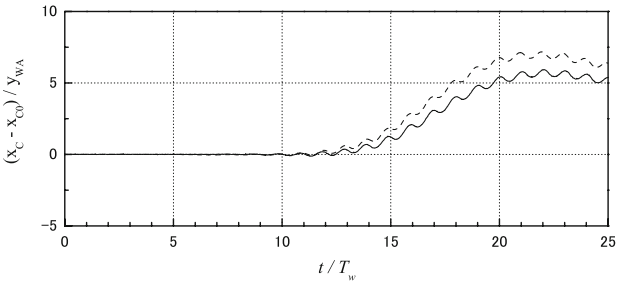

(d) sway

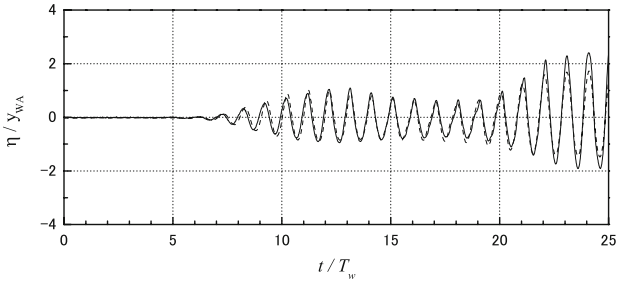

(e) wave elevation

Fig. 24 Comparison of the time histories for $T_w = 1.0$ s, free sway

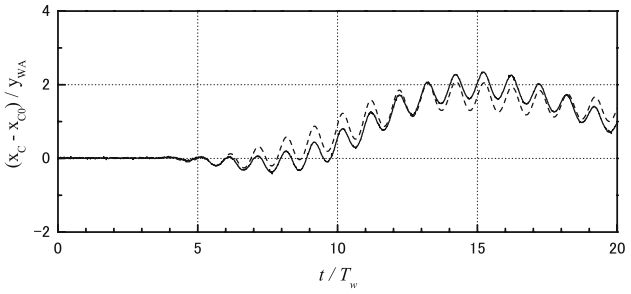

Fig. 25 Sway motion for $T_w = 1.0$; computation with tfriction considered

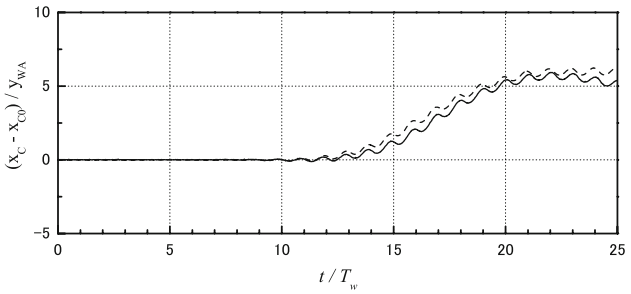

Fig. 26 Sway motion for $T_w = 0.7$; computation with friction considered

the agreement between the computation and the experiment is much better than before for $T_w = 1.0$ and $T_w = 0.7$ s. For heave, roll and wave elevation, introducing mechanical friction effects to the computation did not result in any obvious changes, and so these results are not shown here.

5 Conclusions

In this paper, a two-dimensional wave–body interaction problem was studied by both numerical simulation and experiment. One purpose of this study was to propose a two-dimensional benchmark problem that could be used to validate the CFD code for strongly nonlinear wave–body interactions, in which the water-on-deck phenomenon can be an important factor in the motions of the body. The experimental conditions were simple and both the body motion and the free surface elevation at a particular point are measured and can be easily compared to the results from numerical simulations.

The CIP-based Cartesian grid method used for the numerical simulation is summarized in the paper, and two new features of the method—the THINC scheme and the virtual particle method—are described in detail. The preliminary validation computation, which tackled a dam-breaking problem, showed that the THINC scheme works much better than the original CIP scheme as an interface-capturing scheme in terms of mass conservation and the suppression of interface smearing. The second validation computation, on forced oscillation in heave with a rectangular floating body, enabled us to check the precision of the hydrodynamic force calculation. The computed added-mass and damping coefficients agree well with those obtained experimentally, and it was shown that viscous effects on the damping force can be correctly predicted by the current numerical model.

For the wave–body interaction problem, computations focusing on the experimental problem for two typical periods and with the sway motion either fixed or restrained by a spring were presented. For the fixed-sway case, the water-on-deck phenomenon appears for $T_w = 0.7$ s but not for $T_w = 1.0$ s. In the former case there are nonzero average values for heave and roll, which can be reasonably explained as an effect of the green water by performing a static analysis of the computational results. Upon comparing the body motions and free-surface variations between the numerical and experimental results, it was apparent that there was satisfactory agreement. For the free-sway case, accurate predictions for the body motions were obtained, except for the sway motion when friction was ignored in the experiment setup. Another computation indicated that introducing a frictional force term into the motion equation significantly improves the accuracy of the sway prediction.

References

1. Hu CH, Kashiwagi M (2004) A CIP-based method for numerical simulations of violent free surface flows. J Mar Sci Technol 9: 143–157
2. Hu CH, Kashiwagi M, Kishev Z, Sueyoshi M, Faltinsen O (2006) Application of CIP method for strongly nonlinear marine hydrodynamics. Ship Technol Res 53(2):74–87
3. Yabe T, Xiao F, Utsumi T (2001) The constrained interpolation profile method for multiphase analysis. J Comput Phys 169: 556–593
4. Xiao F, Ikebata A (2003) An efficient method for capturing free boundaries in multi-fluid simulations. Int J Num Methods Fluids 42:187–210
5. Kishev Z, Hu C, Kashiwagi M (2006) Numerical simulation of violent sloshing by a CIP-based method. J Mar Sci Technol 11:111–122
6. Xiao F, Honma Y, Kono T (2005) A simple algebraic interface capturing scheme using hyperbolic tangent function. Int J Numer Methods Fluids 48:1023–1040
7. Hu C, Kashiwagi M (2007) Numerical and experimental studies on three-dimensional water on deck with a modified Wigley model. In: Prepr Proc 9th Int Conf on Numerical Ship Hydrodynamics, Ann Arbor, MI, 5–8 Aug 2007, 1:159–169
8. Godunov SK (1959) Finite difference methods for numerical computation of discontinous solutions of the equations of fluid dynamics. Mat Sbornik 47:271–295
9. Vengatesan V, Varyani KS, Barltrop NDP (2000) Wave–current forces on rectangular cylinder at Low KC Numbers. Int J Offshore Polar Eng 10(4):276–284